crystals

MDPI

Article

Ag_3PO_4/Bi_2WO_6 Heterojunction Photocatalyst with Remarkable Visible-Light-Driven Catalytic Activity

Li Wang [1], Junbo Wang [2,*], Yanfei Fei [1], Heping Cheng [3], Hua Pan [1,*] and Chunfeng Wu [2]

[1] Key Laboratory of Pollution Exposure and Health Intervention of Zhejiang Province, College of Biology and Environmental Engineering, Zhejiang Shuren University, Hangzhou 310015, China; wlll36@163.com (L.W.); yffei16@hotmail.com (Y.F.)
[2] Key Laboratory of Inorganic Functional Materials, School of Chemistry and Chemical Engineering, Huangshan University, Huangshan 245041, China; 22007061014@mail.hsu.edu.cn
[3] School of Information Engineering, Huangshan University, Huangshan 245041, China; chenghp@hsu.edu.cn
* Correspondence: wangjunbo@hsu.edu.cn (J.W.); panhua@zjsru.edu.cn (H.P.); Tel.: +86-571-88297229 (H.P.)

Abstract: Novel Ag_3PO_4/Bi_2WO_6 catalysts with enhanced visible-light performance were synthesized using a hydrothermal method and characterized to investigate their morphology, microscopic structure, and binding energies. Photoluminescence spectrum (PL) and electrochemical impedance spectroscopy (EIS) data demonstrate that the formed Ag_3PO_4/Bi_2WO_6 heterojunction effectively promotes hole (h^+)–electron (e^-) separation and transfer efficiency, resulting in the enhancement of photocatalytic activity. Ag_3PO_4/Bi_2WO_6 displays higher photocatalytic activity than pure Bi_2WO_6 or Ag_3PO_4 alone. Photogenerated holes (h^+), $\cdot O_2^-$, and ·OH were found to be the main active species for the degradation of malachite green (MG), methylene blue (MB), and Rhodamine B (RhB). The DFT calculation explains the photostability of Ag_3PO_4/Bi_2WO_6 from the perspective of electronic structure. The bandgap of Ag_3PO_4/Bi_2WO_6 between the highest occupied molecular orbital (HOMO) and the lowest unoccupied molecular orbital (LUMO) is 1.41 eV, compared with that of Ag_3PO_4 at 0.91 eV and Bi_2WO_6 at 2.59 eV. Ag–O–Bi hybridization and the wide HOMO–LUMO bandgap lead to difficulty in electron transfer. As a consequence, Ag^+ is difficult to obtain electrons and difficult to convert into Ag^0, which makes the catalyst stable.

Keywords: Ag_3PO_4; Bi_2WO_6; heterojunction; photocatalyst; visible-light-driven

check for updates

Citation: Wang, L.; Wang, J.; Fei, Y.; Cheng, H.; Pan, H.; Wu, C. Ag_3PO_4/Bi_2WO_6 Heterojunction Photocatalyst with Remarkable Visible-Light-Driven Catalytic Activity. *Crystals* **2023**, *13*, 1531. https://doi.org/10.3390/cryst13111531

Academic Editor: Dah-Shyang Tsai

Received: 19 September 2023
Revised: 4 October 2023
Accepted: 6 October 2023
Published: 24 October 2023

1. Introduction

In recent years, semiconductor photocatalysis has gained attention as an efficient and environmentally friendly technology for tackling current environmental issues. The photocatalytic process offers several benefits, including simplicity, energy efficiency, and the elimination of organic pollutants, without producing secondary pollution [1–4]. Conventional photocatalysts, including TiO_2 and ZnO, have been extensively researched for their ability to degrade organic pollutants [5]. However, they are limited to absorbing ultraviolet light and cannot fully utilize sunlight [6]. Recently, visible-light-response photocatalysts, such as Bi_2WO_6, BiOBr, $BiVO_4$, $Bi_2O_2CO_3$, Ag_3PO_4, AgBr, Ag_3VO_4, and AgCl, have been widely studied for their capacity to break down toxic dyes and organic pollutants [7–15]. Among these materials, Bi_2WO_6 has garnered significant attention due to its capacity to degrade organic pollutants through visible-light irradiation [16–19]. However, its practical application is thwarted by its high recombination of h^+–e^- pairs and low absorption efficiency of visible light [20–22]. Similarly, the Ag_3PO_4 photocatalyst reveals exceptional potential in photocatalytic processes for organic dye degradation under visible-light irradiation [23,24]. Furthermore, Ag_3PO_4 is a viable option for creating heterostructure composites, effectively enhancing photocatalytic activity. Nevertheless, the overabundance of electrons in the valence band of Ag_3PO_4 may lead to severe photo-corrosion by Ag^+ to Ag^0 [25]. Recently, various methods, including particle size and morphology control [26], metal deposition modification, and doping, have been employed to enhance and optimize the photocatalytic activity and stability of Ag_3PO_4. One promising approach is the coupling of Ag_3PO_4 with Bi_2WO_6. Maryam Amiri et al. developed a Bi_2WO_6/Ag_3PO_4-Ag Z-scheme heterojunction catalyst, which utilized the surface plasmon resonance (SPR) effect of Ag to increase photocatalytic activity and stability [27]. Sittikorn Jonjana et al. discovered that a 10 wt% mixture of Ag_3PO_4/Bi_2WO_6 exhibited superior photocatalytic activity and stability compared with separate Ag_3PO_4 or Bi_2WO_6 samples. This finding highlights the lack of research focused on mixtures exceeding 10 wt% of the Ag_3PO_4/Bi_2WO_6 system [28].

In this study, we present a straightforward hydrothermal and in situ precipitation approach to create a composite photocatalyst of Ag_3PO_4/Bi_2WO_6 with a boosted Ag_3PO_4 concentration. We evaluated the catalytic performance of the obtained samples, described the structural features, and examined the connections between the physicochemical characteristics and catalytic performance. Furthermore, we employed DFT to ascertain the grounds for the stability of Ag_3PO_4/Bi_2WO_6 based on electronic structure analysis.

2. Materials and Methods

2.1. Reagents and Materials

All the reagents used in the experiment were of analytic grade and were commercially purchased without further purification. $AgNO_3$; $NaH_2PO_4 \cdot 3H_2O$; $Bi(NO_3)_3 \cdot 5H_2O$; $Na_2WO_4 \cdot 2H_2O$; Isopropyl alcohol (IPA); and MG, MB, and RhB were obtained from Sinopharm Chemical Reagent. Ammonium oxalate (AO) was purchased from Xilong Chemical Reagent, while p-benzoquinone (BQ) was obtained from Aladdin.

2.2. Preparation of Photocatalysts

In a typical procedure, $Bi(NO_3)_3$ (2 mmol, 0.7899 g) was dissolved in 10 mL of glacial acetic acid and 10 mL of 2 mol/L HNO_3 to prevent Bi^{3+} ion hydrolysis. Technical term abbreviations were explained when they were first used. Afterward, 1 mmol of Na_2WO_4 (20 mL) solution was gradually added dropwise to the $Bi(NO_3)_3$ solution. The mixture was continuously stirred for 4 h, then moved to a Teflon-coated autoclave and maintained at 160 °C for 20 h. Finally, it was cooled down to room temperature naturally. The Bi_2WO_6 obtained was washed several times with deionized water to eliminate any residual by-products or reactants. It was then dried at 80 °C for 24 h. The dried powder was further calcined in a muffle oven at a temperature of 400 °C for 12 h with a temperature elevator of 5 °C/min.

Ag_3PO_4/Bi_2WO_6 composites were prepared using an in situ precipitation method. Typically, 0.6977 g (1 mmol) of the previously obtained Bi_2WO_6 powder was dispersed into 40 mL of deionized water via ultrasound for 30 min. Next, 20 mL of $AgNO_3$ solution (0.5096 g, 3 mmol) was added to the Bi_2WO_6 dispersion. Subsequently, the mixture was stirred for an hour; then, 20 mL of NaH_2PO_4 solution (0.1199 g, 1 mmol) was added dropwise with magnetic stirring. Finally, the resulting precipitate underwent washing with deionized water several times, centrifugation, and vacuum drying at 60 °C. Pure Ag_3PO_4, Bi_2WO_6, and Ag_3PO_4/Bi_2WO_6 mixed composites were also synthesized following identical procedures for comparative analysis. Ag_3PO_4/Bi_2WO_6-9 indicates that the mass proportion of Ag_3PO_4 is 90%. Meanwhile, Ag_3PO_4/Bi_2WO_6-X with various mass proportions (90%, 80%, 70%, 60%, and 50%) was produced alike by controlling the Ag_3PO_4 dose. The resulting products were labeled as Ag_3PO_4/Bi_2WO_6-X, where X equals 9, 8, 7, 6, and 5, respectively.

2.3. Characterization

The crystal phases and structures of the samples were analyzed via powder X-ray diffraction (XRD) utilizing a D/max-2550 PC (RIGAKU, Tokyo, Japan) equipped with Cu Kα (λ = 1.54056 Å) radiation, set at 40 kV and 200 mA, and scanned from 15° to 85° at a rate of 6 °/min. The Thermo ESCALAB 250 X-ray photoelectron spectroscope (XPS, Thermo Fisher Scientific, Waltham, MA, USA) was used to assess surface chemical compositions. Additionally, morphologies were examined using a Hi-tachi S-4800 field emission microscope. The scanning electron microscope (FE-SEM) from Japan operated at 10 kilovolts for imaging. The High-Resolution Transmission Electron Microscopy (HR-TEM) images were obtained utilizing a JEOL JEM-2100F microscope from Tokyo, Japan. To determine the energy band structure of the photocatalysts, UV–visible Optical Diffuse Reflectance Spectra (DRS) were measured using Ba_SO_4 as the background with a PerkinElmer Lambda850 instrument from MA, USA. The PerkinElmer LS55 MA USA's PL spectra, with an excitation wavelength of 360 nm, evaluated the h^+–e^- pairs' recombination degree.

The CHI660E Electrochemical Workstation (CH Instruments, Shanghai, China) measured the photocatalyst's Electrochemical Impedance Spectroscopy (EIS) over a 100 Hz to 0.01 kHz frequency domain with a 5 mV perturbation potential. The EIS outcomes were fitted with Zview 3.0 software. The electrochemical electrode is constructed with a photocatalyst (approximately 3 mg in ethanol) deposition on an indium tin oxide glass, which serves as the working electrode. A Pt sheet acts as the counter electrode, a saturated calomel electrode (SCE) is used as the reference electrode, and a 0.1 M Na_2SO_4 solution acts as the electrolyte solution. For slight and viscous suspension solutions, 3 mg sample powders mixed with Nafion ionomer were dissolved in an ethanol aqueous solution. The suspension was evenly applied onto the clean electrode surface composed of indium-tin oxide (ITO) through drop-coating and left to air dry, according to reference [23].

2.4. Activity Test

Photocatalytic experiments were conducted using a slurry reaction reactor and a 500 W Xe lamp (300 mW/cm^2) from Perfectlight Technology Co., Ltd., Beijing, China, which was equipped with a cutoff filter (>400 nm) as a visible-light source. The target pollutants used were Malachite Green (MG), Methylene Blue (MB), and Rhodamine B (RhB) dye, and 20 mg of photocatalyst was dispersed into 50 mL of pollutant solution (C = 10 mg/L, MG, MB, or RhB) under visible-light irradiation at 25 °C. Before irradiation, the suspension was stirred continuously in the dark for 30 min to create a finely dispersed solution and establish adsorption–desorption equilibrium. While being irradiated, each 0.5 mL suspension was collected in a plastic sample tube containing 2.5 mL deionized water every 10 min and then centrifuged. The supernatant was analyzed using a T9 UV–vis spectrophotometer. Figure 1 depicts the schematic diagram of the photocatalytic reactor.

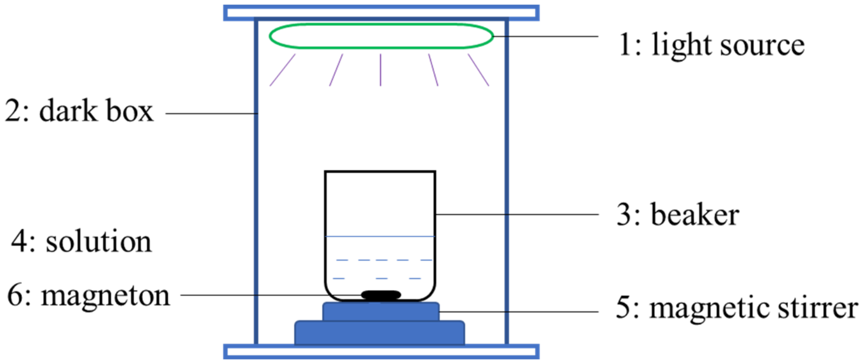

Figure 1. The schematic diagram of photocatalytic reactor.

2.5. Calculation

DFT calculations were conducted using plane wave methods. We employed the Cambridge Sequential Total Energy Package (CASTEP) to perform the calculations. Our computational models consisted of tetragonal supercells (2 × 2 × 1) of Ag_3PO_4 and Bi_2WO_6. The Broyden–Fletcher–Goldfarb–Shanno (BFGS) algorithm was utilized to optimize the lattice constants and atomic coordinates in these supercells. Subsequently, after acquiring the stable structure, we calculated the electronic properties of both supercells. The study utilized Generalized Gradient Approximation (GGA) to express exchange and correlation effects, which were parameterized by the PBE function developed by Perdew–Burke–

Ernzerhof. Interactions between core and valence electrons were described using an ultrasoft pseudopotential. All geometry optimizations employ convergence thresholds of 5×10^{-6} eV/atom for total energies, a maximum force of 0.01 eV/Å, a maximum stress of 0.02 GPa, and a maximum displacement of 5×10^{-4} Å. Default values were utilized for other calculation parameters.

3. Results and Discussion

3.1. Physicochemical Structure

Figure 2 displays X-ray diffraction (XRD) patterns for various Ag_3PO_4, Bi_2WO_6, and Ag_3PO_4/Bi_2WO_6 samples with varying ratios. The pure Ag_3PO_4 exhibits a cubic phase (JCPDS: 06-0505). The diffraction peaks of Ag_3PO_4 match crystal planes of (110), (200), (210), (211), (220), (310), (222), (320), (321), (400), (420), (421), and (332) at 2θ = 20.91°, 29.75°, 33.24°, 36.46°, 42.54°, 47.80°, 52.69°, 54.87°, 55.02°, 61.58°, 69.91°, 71.88°, and 73.88°, respectively, as depicted in Figure 2 [29]. The pure Bi_2WO_6 crystal (JCPDS 39-0256) can be clearly identified as orthorhombic. The perfectly matching characteristic peaks at 2θ = 28.29°, 32.79°, 47.14°, 55.99°, 58.54°, 68.75°, 76.08°, and 78.53° with Bi_2WO_6 (JCPDS No. 39-0256, space group: Pbca) can be indexed to the (131), (200), (202), (133), (262), (400), (193), and (204) crystal planes of orthorhombic Bi_2WO_6 [30,31], respectively. All diffraction peaks of Bi_2WO_6, Ag_3PO_4, and Ag_3PO_4/Bi_2WO_6 composites exhibit a well-matched two-phase composition. None of the diffraction peaks for impurities like Ag, Ag_2O, Bi_2O_3, or WO_3 are observed. The strong and sharp peaks assigned to Ag_3PO_4/Bi_2WO_6 composites display favorable crystal structures. Notably, the peak position of Ag_3PO_4 remains relatively unchanged, indicating that Bi_2WO_6 only adheres to the surface of Ag_3PO_4 without penetrating the lattice.

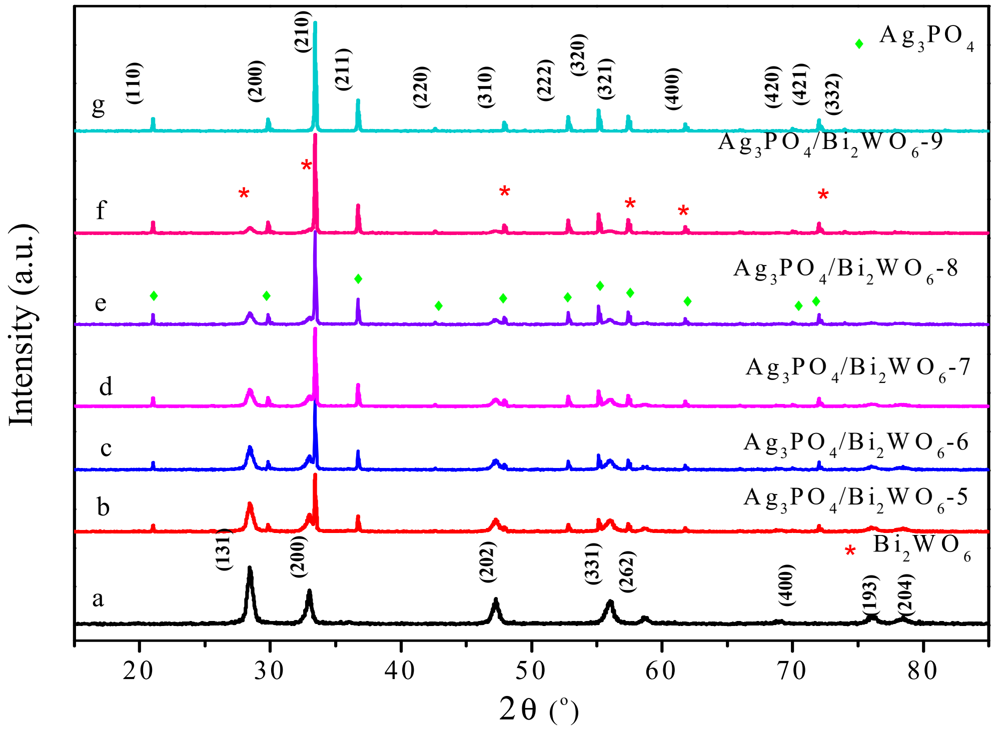

Figure 2. The X-ray diffraction patterns obtained for the samples prepared with varying Ag_3PO_4/Bi_2WO_6 ratios. The asterisk symbol (*) indicates the Bi_2WO_6 peak positions, while the diamond symbol (◆) represents the peak positions of Ag_3PO_4.

The SEM was used to characterize the morphology and microscopic structure of the as-prepared samples, including Ag_3PO_4, Bi_2WO_6, and Ag_3PO_4/Bi_2WO_6-9. In Figure 3a,b, Ag_3PO_4 exhibits cubic-shaped nanoparticles ranging between 100 and 400 nm in diameter, while the Bi_2WO_6 sample presents an irregular cubical shape between 30 and 100 nm. The SEM image of Ag_3PO_4/Bi_2WO_6-9 shows that the Bi_2WO_6 nanoparticle tightly adheres to the surface of Ag_3PO_4 (Figure 3c). Figure 3d displays the TEM pattern of Ag_3PO_4/Bi_2WO_6-9. The regular shape of the material is Ag_3PO_4, while the amorphous shape is usually Bi_2WO_6. An amplified image of the local area can be found in Figure 3e, which highlights the heterojunction between Ag_3PO_4 and Bi_2WO_6 within a green frame. The magnified part of the interface is displayed in Figure 3f. Additionally, the HR-TEM pattern of Ag_3PO_4 in Ag_3PO_4/Bi_2WO_6-9 heterojunction can be found in Figure 3g. The lattice fringe of 0.246 nm corresponds to the (211) plane of cubic Ag_3PO_4 phase and coincides well with reported literature [32]. The HR-TEM image of Bi_2WO_6 is shown in Figure 3h. The particle is confirmed to be Bi_2WO_6 with space group B2cb [33] by the (200) crystal spacing (0.273 nm). In Figure S1, the elemental maps of Ag_3PO_4, Bi_2WO_6, and Ag_3PO_4/Bi_2WO_6-9 demonstrate uniform distribution of all elements without agglomeration.

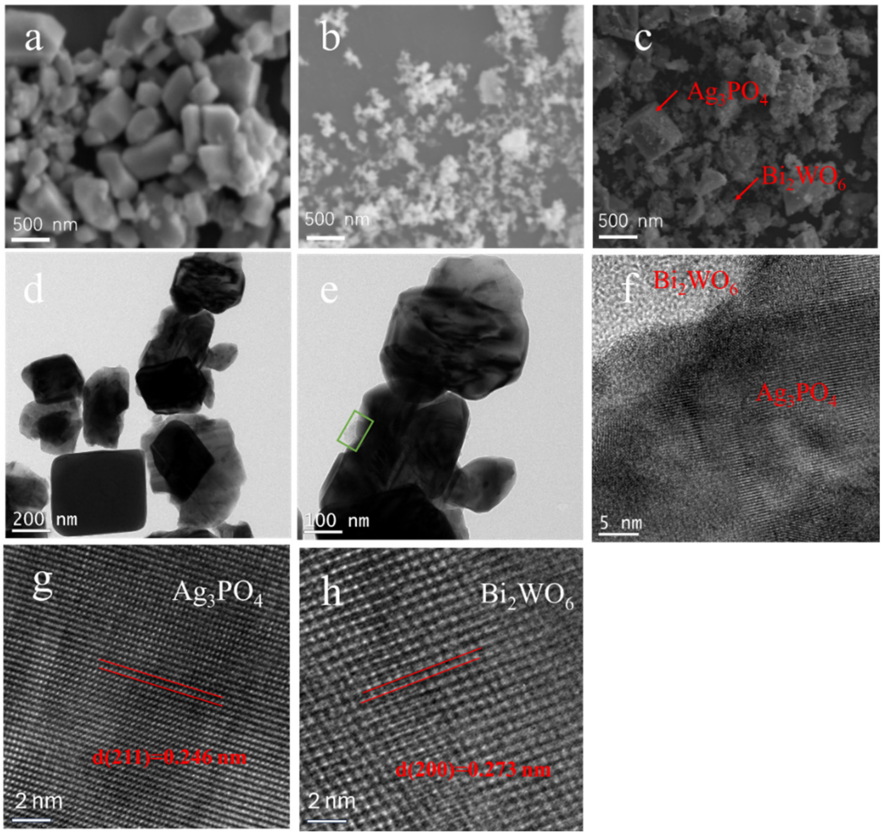

Figure 3. (**a**) SEM of Ag_3PO_4; (**b**) SEM of Bi_2WO_6; (**c**) SEM image of Ag_3PO_4/Bi_2WO_6-9; (**d**) TEM image of Ag_3PO_4/Bi_2WO_6-9; (**e**) magnified TEM image ofAg_3PO_4/Bi_2WO_6-9; (**f**) HR-TEM of Ag_3PO_4/Bi_2WO_6-9 heterojunction structure; (**g**) HR-TEM of Ag_3PO_4 in Ag_3PO_4/Bi_2WO_6-9; (**h**) HR-TEM of Bi_2WO_6 in Ag_3PO_4/Bi_2WO_6-9.

XPS was utilized to determine the electronic structures of Ag_3PO_4, Bi_2WO_6, and Ag_3PO_4/Bi_2WO_6-9 composites. Figure 4a displays the XPS spectra of Ag 3*d* for both the Ag_3PO_4 and Ag_3PO_4/Bi_2WO_6-9 composite catalysts. The characteristic peaks of Ag 3*d* at 368.0 eV (Ag $3d_{5/2}$) and 374.0 eV (Ag $3d_{3/2}$) are attributed to the Ag^+ ions in Ag_3PO_4. After the introduction of Bi_2WO_6, the binding energy of spin-orbit Ag 3*d* splits into two peaks at 368.3 and 374.3 eV, which is 0.3 eV higher than that of Ag_3PO_4. This indicates that the electronic clouds on Ag^+ in Ag_3PO_4 shift to Bi_2WO_6 after combination. Furthermore, compared with pure Ag_3PO_4, the binding energy of P 2*p* in Ag_3PO_4/Bi_2WO_6-9 is higher, with a value of 133.7 eV instead of 132.9 eV (Figure 4b). The peaks observed at 159.4 eV and 164.7 eV correspond to the Bi $4f_{7/2}$ and Bi $4f_{5/2}$ sublevels of Bi_2WO_6, respectively. On the other hand, the peaks at 159.9 eV and 165.2 eV are associated with the Bi $4f_{7/2}$ and Bi $4f_{5/2}$ levels of Ag_3PO_4/Bi_2WO_6-9, respectively, suggesting that the bismuth species in the composite are Bi^{3+} cations. Furthermore, the peaks observed at 35.98 eV and 37.98 eV for the W $4f_{7/2}$ and W $4f_{5/2}$ sublevels, respectively, can be attributed to a six-valent oxidation state for W^{6+} in Ag_3PO_4/Bi_2WO_6-9. These findings indicate a 0.18 eV deviation of $4f_{7/2}$ and $4f_{5/2}$ levels relative to the values in pure Bi_2WO_6 (refer to Figure 4d for more details).

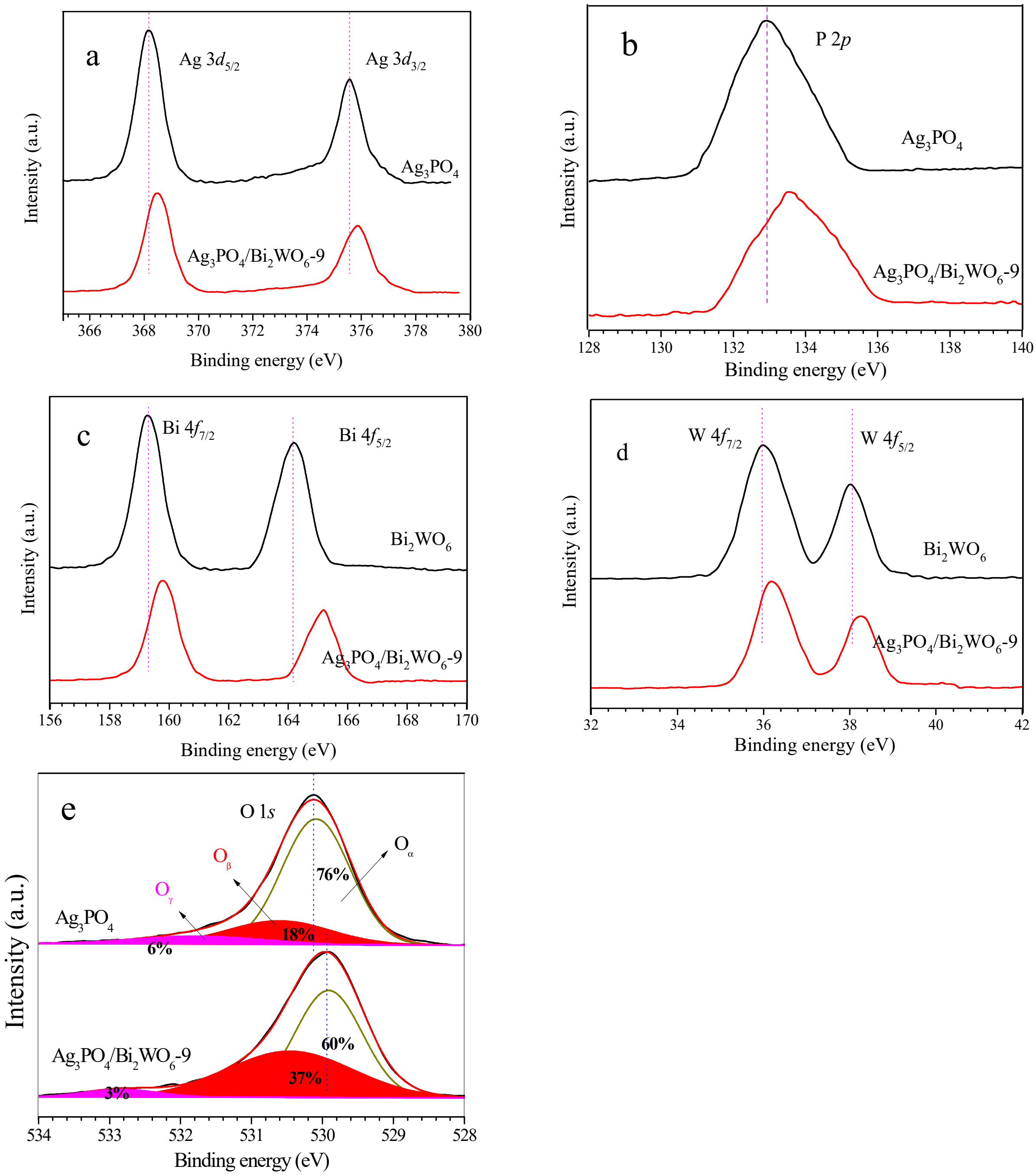

Figure 4. XPS spectra of the catalysts. (**a**) Ag 3*p*; (**b**) P 2*p*; (**c**) Bi 4*f*; (**d**) W 4*f*; (**e**) O 1*s*.

The O 1*s* XPS spectra for the samples are presented in Figure 4e. The spectra for Ag_3PO_4 indicate three distinct peaks with binding energies of 530.1 eV (identified as O_α), 531.6 eV (531.3 eV, identified as O_β), and 533.1 eV (533.1 eV, identified as O_γ). These peaks are attributed to lattice oxygen, adsorbed oxygen species, and defect oxygen located on the surface of Ag_3PO_4, respectively [33–35]. In the case of Ag_3PO_4/Bi_2WO_6-9, the binding energies for O 1*s* orbits are 529.9 eV, 531.4 eV, and 532.8 eV. The composites also exhibit significantly lower energy shifts compared to their individual constituents. It is apparent that the $(O_\beta + O_\gamma)/O_\alpha$ ratio of Ag_3PO_4 (24%:76%) is appreciably lower than that of the Ag_3PO_4/Bi_2WO_6-9 composite (40%:60%). The augmented ratio of active oxygen $(O_\beta + O_\gamma)$ is beneficial in enhancing photocatalytic performance. The chemical interactions between Bi_2WO_6 and Ag_3PO_4 have resulted in variations in the binding energies of Ag 3*d*, P 2*p*, Bi 4*f*, W 4*f*, and O 1*s*, indicating the formation of heterostructures and the promotion of interfacial charge transfer. As a result, the photocatalytic activity of Ag_3PO_4/Bi_2WO_6 nanocomposites has improved. An increase in binding energy typically leads to the loss of an atom's charge and a subsequent decrease in the density of the surrounding electron cloud. This reduction enhances the attraction between the nucleus and electrons, thereby increasing the electron binding energy. This leads to an increase in reactive oxygen species and a decrease in electron density of Ag^+ ions, ultimately improving the catalytic performance and stability of Ag_3PO_4.

UV–vis DRS was conducted to examine the optical properties of relevant samples. All samples displayed visible-light absorbance. Figure S2 displays the results of UV–vis DRS for Bi_2WO_6, Ag_3PO_4, and Ag_3PO_4/Bi_2WO_6 with differing composite ratios. Ag_3PO_4/Bi_2WO_6 exhibits varying absorption band edges according to the composite ratio. The composites demonstrate notable absorption within the visible-light range (760 nm > λ > 400 nm). In Figure 5, the fundamental absorption band edge of pure Bi_2WO_6 is measured at 459 nm. Additionally, the strong absorption band edge of Ag_3PO_4 is observed at approximately 523 nm, in line with previous findings [29]. The absorption of the composite material Ag_3PO_4/Bi_2WO_6-9 demonstrates infrared transfer to 493 nm compared with Bi_2WO_6. Based on Figure 5a, the direct optical band gap energies (E_g) of pure Bi_2WO_6, Ag_3PO_4, and Ag_3PO_4/Bi_2WO_6-9 composites are estimated at 2.70, 2.37, and 2.51 eV, respectively. Tauc plots of Bi_2WO_6, Ag_3PO_4, and Ag_3PO_4/Bi_2WO_6-9 are displayed in Figure 5b for better comprehension. This demonstrates the formation of heterostructure in Ag_3PO_4/Bi_2WO_6-9.

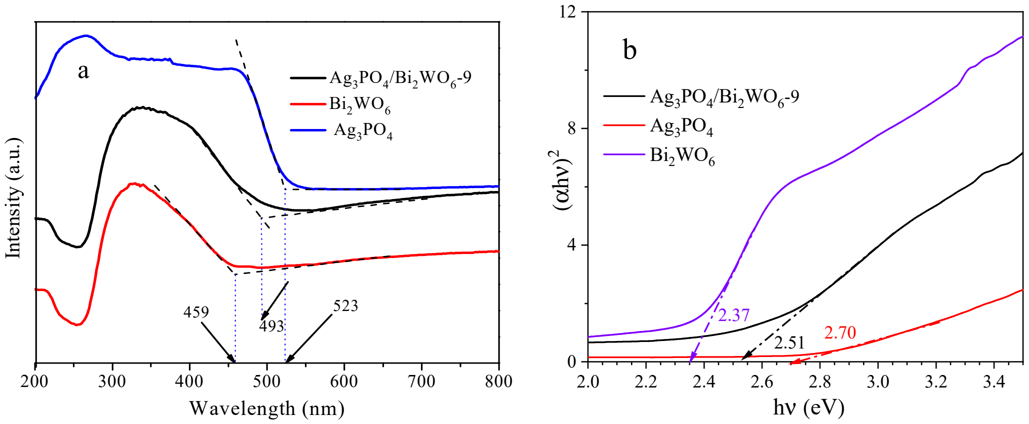

Figure 5. (**a**) UV–vis DRS of as-synthesized samples of Bi_2WO_6, Ag_3PO_4, and Ag_3PO_4/Bi_2WO_6-9. (**b**) Tauc plots of Bi_2WO_6, Ag_3PO_4, and Ag_3PO_4/Bi_2WO_6-9.

3.2. Photocatalytic Performance under Visible-Light Irradiation

The catalytic performances of visible-light-driven catalysts were evaluated through the degradation of aqueous dyes with different structures, including triphenylmethane MG, phenothiazine group MB, and triphenyl RhB. To ensure adsorption–desorption equilibrium, the mixture containing dye solution and catalyst was kept in the dark for 30 min before irradiation. As depicted in Figure 6(a_1,b_1,c_1), Ag_3PO_4/Bi_2WO_6-9 shows a good adsorption capacity for MG, MB, and RhB.

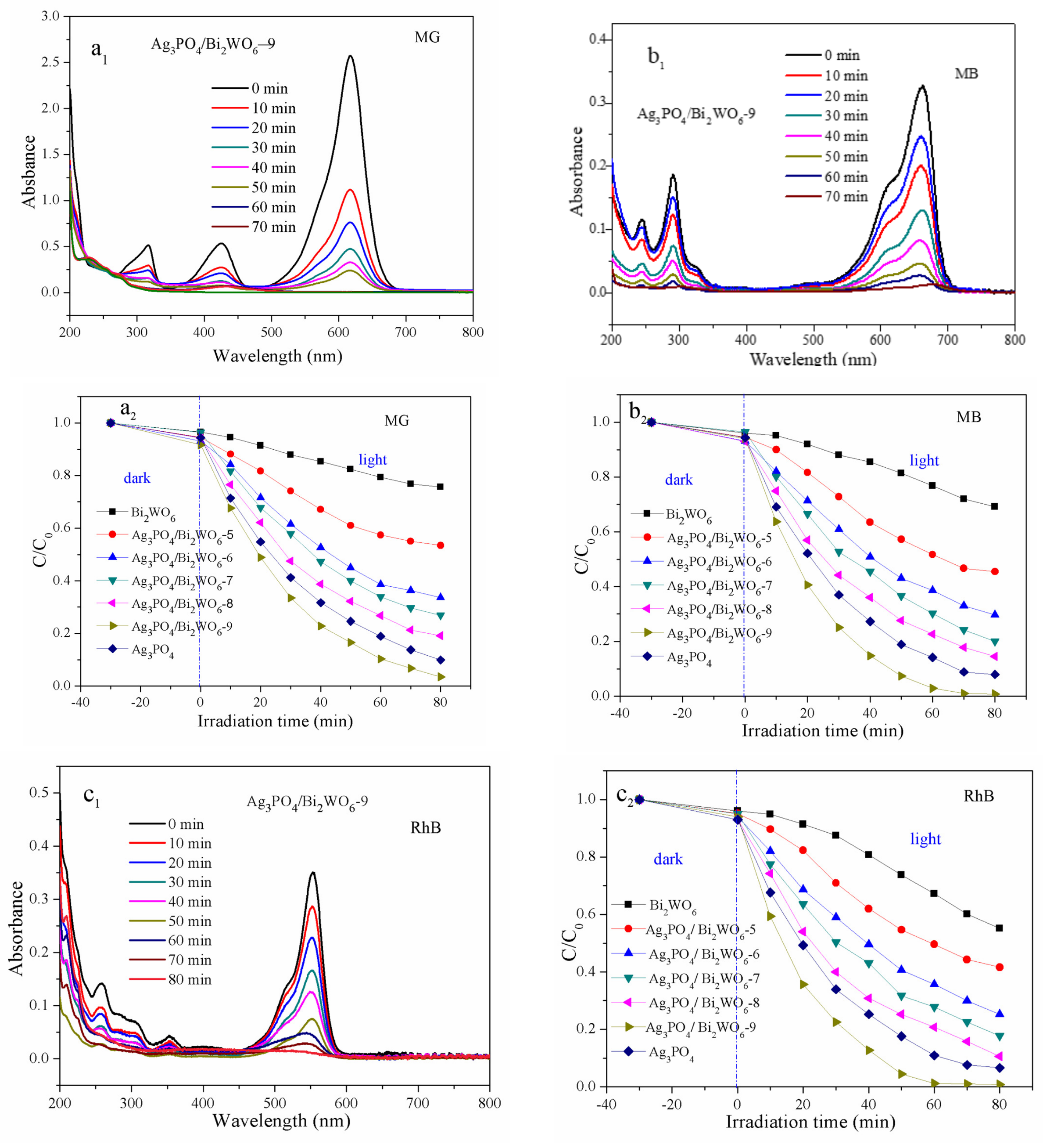

Figure 6. (**1**) Time-dependent UV–vis absorption spectra of the MG (**a$_1$**), MB (**b$_1$**), and RhB (**c$_1$**) solution in the presence of Ag_3PO_4/Bi_2WO_6-9. (**2**) Degradation curves of MG (**a$_2$**), MB (**b$_2$**), and RhB (**c$_2$**) with Ag_3PO_4, Bi_2WO_6, and Ag_3PO_4/Bi_2WO_6 composites under visible-light irradiation.

Figure 6(a$_2$,b$_2$,c$_2$) display the decolorization efficiencies of Ag_3PO_4/Bi_2WO_6-X (X = 5, 6, 7, 8, 9), pure Ag_3PO_4, and Bi_2WO_6 for the dyes MG, MB, and RhB. The activity of these catalysts follows the trend of Bi_2WO_6 < Ag_3PO_4/Bi_2WO_6-5 < Ag_3PO_4/Bi_2WO_6-6 < Ag_3PO_4/Bi_2WO_6-7 < Ag_3PO_4/Bi_2WO_6-8 < Ag_3PO_4 < Ag_3PO_4/Bi_2WO_6-9 for the three dyes. The photocatalytic activity of the Ag_3PO_4/Bi_2WO_6-9 composite displays the best catalytic performance.

The stability of Ag_3PO_4 and Ag_3PO_4/Bi_2WO_6-9 was assessed by studying the degradation of RhB dyes under visible-light irradiation (see Figure 7). Following five cycles of the photodegradation process, the degradation efficiency of Ag_3PO_4 decreased from 86% to 30%. In contrast, the degradation efficiency of Ag_3PO_4/Bi_2WO_6-9 decreased from 97% to 76%, indicating that Ag_3PO_4/Bi_2WO_6-9 displays little activity loss and good photochemical stability. In contrast, the degradation efficiency of Ag_3PO_4/Bi_2WO_6-9 decreased from 97% to 76%, indicating that Ag_3PO4/Bi_2WO_6-9 displays little activity loss and good photochemical stability.

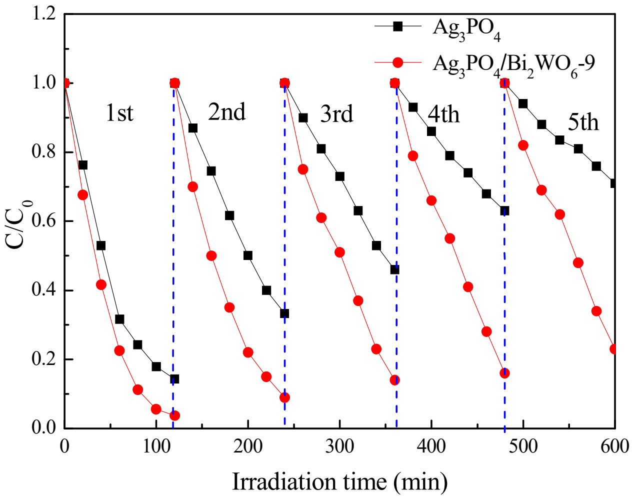

Figure 7. Photocatalytic cycle performance of Ag_3PO_4 andAg_3PO_4/Bi_2WO_6-9.

3.3. *The Relationship of Structure and Activity*

3.3.1. Main Free Radicals

Ag_3PO_4/Bi_2WO_6-9 was utilized to photodegrade RhB, and scavengers—namely, AO, IPA, and BQ—were applied to test the ·OH, h^+, and·O_2^- free radicals, correspondingly. Photodegradation efficiencies with different scavengers are presented in Figure 8a. Notably, the efficiency of Ag_3PO_4/Bi_2WO_6-9 without any scavengers is high, while the efficiencies decrease after adding scavengers. Figure 8b displays the reaction rate constant k. Based on the aforementioned results, the primary free radicals were ·OH, while the other free radicals consisted of ·O_2^- and hole. These highly reactive free radicals are potentially accountable for the deterioration of RhB.

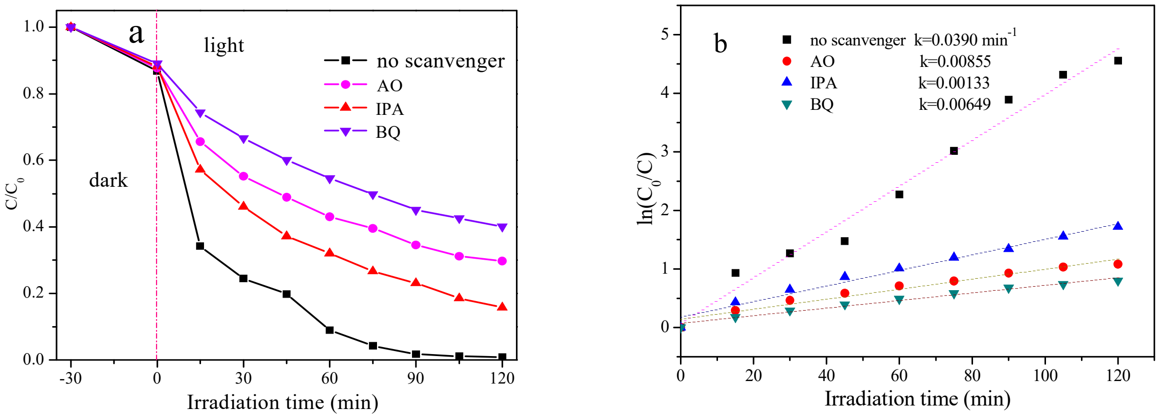

Figure 8. Photodegradation efficiencies of RhB as a function of irradiation time with different scavengers. (**a**) Photodegradation efficiencies with different scavengers. (**b**) Reaction rate constants k with different scavengers.

3.3.2. PL Analysis

Figure S3 displays the photoluminescence (PL) spectra of Ag_3PO_4, Ag_3PO_4/Bi_2WO_6-5, Ag_3PO_4/Bi_2WO_6-6, Ag_3PO_4/Bi_2WO_6-7, Ag_3PO_4/Bi_2WO_6-8, Ag_3PO_4/Bi_2WO_6-9, and Bi_2WO_6 composites. The PL intensities follow the order Bi_2WO_6 > Ag_3PO_4/Bi_2WO_6-5 > Ag_3PO_4/Bi_2WO_6-6 > Ag_3PO_4/Bi_2WO_6-7 > Ag_3PO_4/Bi_2WO_6-8 > Ag_3PO_4/Bi_2WO_6-9 > Ag_3PO_4. The PL intensity of the Ag_3PO_4/Bi_2WO_6-9 composite exhibits an obvious decrease compared with pure Bi_2WO_6 (as shown in Figure 9). The Ag_3PO_4/Bi_2WO_6-9 composite exhibits a decreased PL intensity compared with Ag_3PO_4 and Bi_2WO_6, suggesting efficient inhibition of photoexcited electron–hole recombination through the formation of the Ag_3PO_4/Bi_2WO_6 heterojunction.

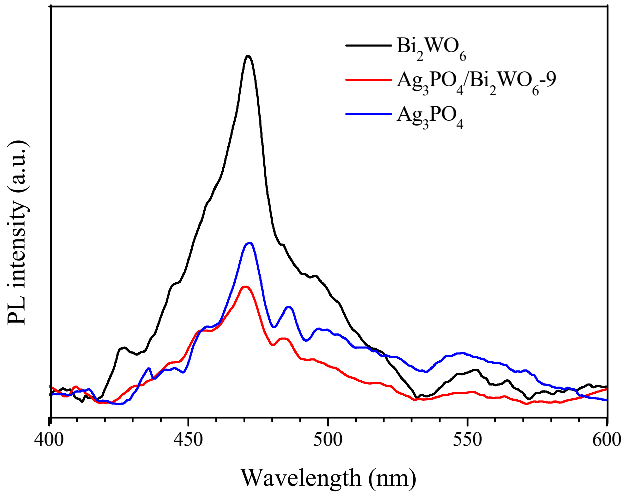

Figure 9. PL spectra of Bi_2WO_6, Ag_3PO_4, and Ag_3PO_4/Bi_2WO_6-9 composites.

3.3.3. EIS Analysis

EIS was utilized to examine the charge transfer resistance and segregation of photogenerated h^+–e^- pairs at solid/electrolyte interfaces in the photocatalyst. Figure 10 illustrates the EIS Nyquist plots of Ag_3PO_4, Bi_2WO_6, and Ag_3PO_4/Bi_2WO_6-9 blends under visible-light irradiation. The corresponding circuit model employed to fit the obtained data is included, where R_s indicates solution resistance, CPE denotes the constant phase angle element, and R_{ct} refers to reaction resistance. This is indicated by the smallest arc radius belonging to Ag_3PO_4/Bi_2WO_6-9. In Figure 10a, the EIS plot shows that Ag_3PO_4/Bi_2WO_6-9 had the fastest interfacial electron transfer and more separation of photogenerated h^+–e^- pairs compared with Bi_2WO_6 and Ag_3PO_4. The simulated data can be found in Table S1. The combination of PL and EIS data indicates that creating a Ag_3PO_4/Bi_2WO_6 heterojunction effectively enhances charge separation and transfer efficiency, consequently resulting in an improvement in photocatalytic activity.

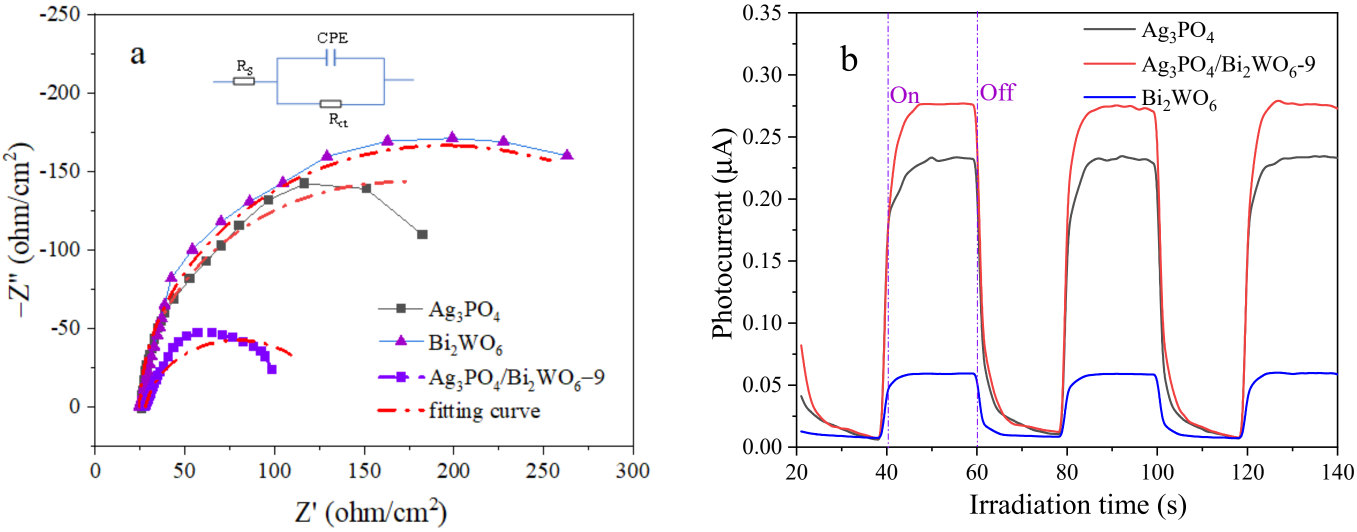

Figure 10. (**a**) EIS plots of the samples under irradiation with visible light. Insert: equivalent circuit used to fit the data; (**b**) transient photocurrent response curves for the three catalysts.

Figure 10b illustrates the transient photocurrent response of the three catalysts, measured over several intermittent irradiation cycles. Upon activation, the photocurrent rapidly increases to a stable current platform, which subsequently falls back to a small value once deactivated. Notably, the photocurrent observed for Ag_3PO_4/Bi_2WO_6-9 is the largest, followed by Ag_3PO_4, while that of Bi_2WO_6 is the smallest. These results suggest that more electrons and holes in Ag_3PO_4/Bi_2WO_6-9 are excited, whereby they subsequently participate in the photocatalytic degradation reaction.

3.3.4. DFT Analysis

To elucidate the electronic states of the catalytically active sites (CASs) in Ag_3PO_4/Bi_2WO_6, the density of states (DOS) of Ag_3PO_4, Bi_2WO_6, and Ag_3PO_4/Bi_2WO_6 were calculated using DFT. Figure S4 illustrates simplified models (unit cell) depicting the crystal structures of Ag_3PO_4 (Figure S4a) and $Bi_2W_2O_6$ (Figure S4b), with different elements represented by distinct colors. The simplified models are solely utilized to demonstrate the bonding environment of Ag_3PO_4 and $Bi_2W_2O_6$. By optimizing the lattice constants, the Ag_3PO_4 and $Bi_2W_2O_6$ supercells have dimensions of 6.026 Å × 6.026 Å × 6.026 Å and 5.5340 Å × 5.4998 Å × 16.5507 Å, respectively. Technical terms are clearly explained when first used. Each P atom coordinates with four O atoms, and each O atom coordinates with one P atom and three Ag atoms in Ag_3PO_4 (Figure 11a).

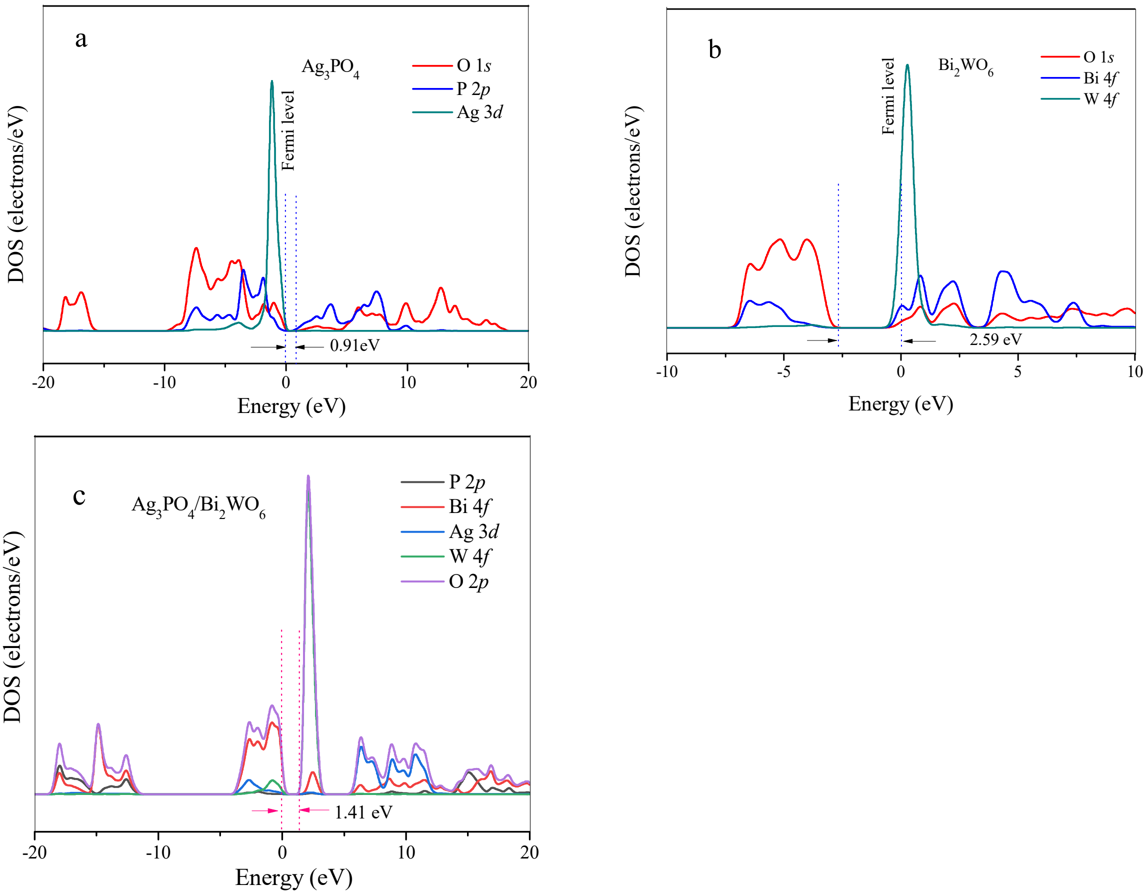

Figure 11. The DOS patterns. (**a**) Ag_3PO_4; (**b**) Bi_2WO_6; (**c**) Ag_3PO_4/Bi_2WO_6.

The DOS of O 1*s*, P 2*p*, and Ag 3*d* appear in the same energy regions, indicating the presence of Ag-O and P-O hybridization. The bandgap between the HOMO and LUMO is approximately 0.91 eV. Mixing with Bi_2WO_6 (Figure 11b) caused an increase in the bandgap to 1.41 eV due to the upshift of HOMO energy (Figure 11c). This tendency is consistent with experimental results showing that the band gap energies of pure Ag_3PO_4, Bi_2WO_6, and Ag_3PO_4/Bi_2WO_6 composites are 2.37, 2.7, and 2.51 eV, respectively. Therefore, due to the hybridization between Ag, O, and Bi, and the wide bandgap between the HOMO and LUMO, the transfer of electrons through bridging O between Ag and Bi may be hindered, resulting in difficulty obtaining electrons to reduce Ag^+ into Ag^0. Additionally, there is implicit hybridization between Bi and W cations through their interactions with bridging O atoms, as the DOS of Bi, O, and W in Bi_2WO_6 are in similar energy regimes. Due to the hybridization of Bi–O–W and the wide bandgap between the HOMO and LUMO, the transfer of electrons between W and Bi through the bridging O is expected to become relatively easy, resulting in the co-existence of multiple oxidation states of W and Bi. The composite Ag_3PO_4/Bi_2WO_6 increases the bandgap between the HOMO and LUMO, thereby enhancing the catalytic activity of the active O and improving the photostability of Ag_3PO_4.

3.3.5. Proposed Photocatalytic Degradation Mechanism

Based on the experimental data and literature review, we propose a mechanism for photocatalysis under visible-light irradiation (see Figure 12). When the catalyst is exposed to visible light, the electrons in the valence band (VB) of Ag_3PO_4 become excited and move to its conduction band (CB) orbital. Consequently, holes are formed in the VB of Ag_3PO_4, while the CB orbital of Ag_3PO_4 becomes occupied by electrons. The same behavior is observed in Bi_2WO_6. The efficient heterojunction between Ag_3PO_4 and Bi_2WO_6 results from the transfer of holes from Bi_2WO_6 to the VB orbital of Ag_3PO_4 and the migration of electrons from Ag_3PO_4 to the CB orbital of Bi_2WO_6. This can be attributed to the lower VB energy level of Ag_3PO_4 compared with that of Bi_2WO_6. Thus, the two materials are tightly bonded together. Furthermore, the dissolved oxygen molecules in water scavenge the electrons present on Ag_3PO_4 CB and produce highly oxidative $\cdot O_2^-$ species, which could react with H_2O to generate ·OH. The hole h+ also produces ·OH after reacting with water, while the formed ·OH, $\cdot O_2^-$, and h^+ effectively break down organic substrates.

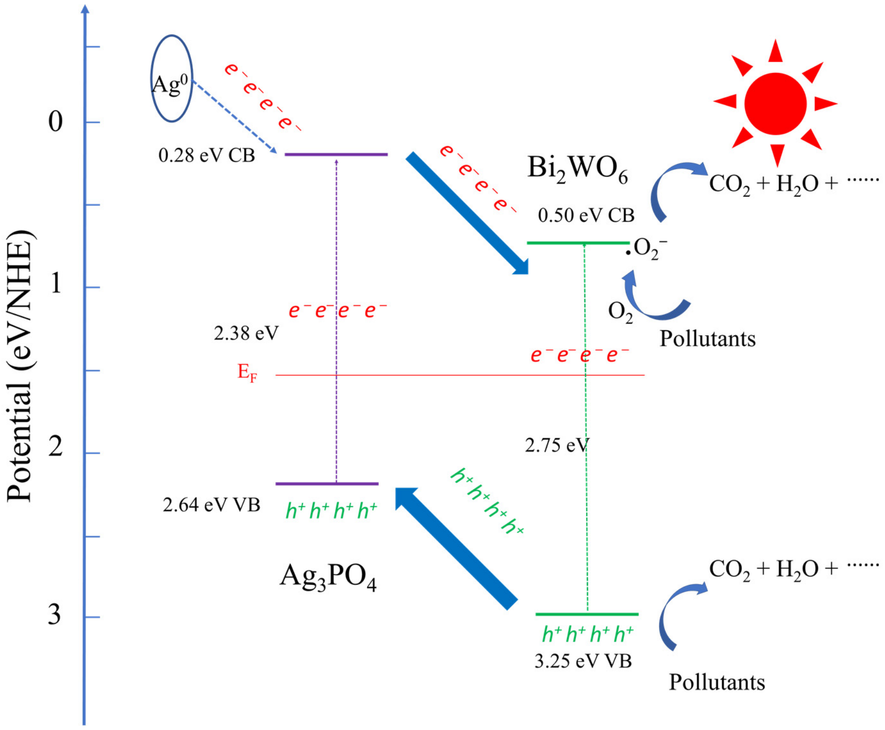

Figure 12. Schematic diagram of the separation and transfer of photogenerated charges in the hybrid under visible-light irradiation.

4. Conclusions

A novel visible-light-driven photocatalyst composed of Ag_3PO_4/Bi_2WO_6 composites was synthesized and characterized successfully. X-ray diffraction analysis demonstrated that the Ag_3PO_4/Bi_2WO_6 composites possess crystal structures. The morphology and microscopic structures of Ag_3PO_4/Bi_2WO_6 were observed through scanning and transmission electron microscopy. X-ray photoelectron spectroscopy exhibited that the catalytic performance and stability of Ag_3PO_4 improved due to an increase in reactive oxygen species and a decrease in the electron density of Ag^+ ions. The Ag_3PO_4/Bi_2WO_6 composites prepared demonstrate superior photodegradation activity for degrading MG, MB, and RhB in comparison with Bi_2WO_6 or Ag_3PO_4 under visible-light irradiation. The improved activity can be attributed to the effective separation of electron–hole pairs generated by light and the production of free radicals such as $\cdot OH$, $\cdot O_2^-$, and h^+.

Supplementary Materials: The following supporting information can be downloaded at: https://www.mdpi.com/article/10.3390/cryst13111531/s1, Table S1. The EIS simulated data for Ag_3PO_4, Bi_2WO_6, and Ag_3PO_4/Bi_2WO_6-9. Figure S1. (**a**) Elemental mapping of Ag_3PO_4; (**b**) elemental mapping of Bi_2WO_6; (**c**) elemental mapping of Ag_3PO_4/Bi_2WO_6-9. Figure S2. UV–vis DRS of Bi_2WO_6, Ag_3PO_4, and Ag_3PO_4/Bi_2WO_6 composites with various ratios. Figure S3. PL spectra of Bi_2WO_6, Ag_3PO_4, and Ag_3PO_4/Bi_2WO_6 composites with various ratios. Figure S4. Crystal structures. (**a**) Ag_3PO_4; (**b**) $Bi_2W_2O_6$.

Author Contributions: Conceptualization, J.W.; data curation, J.W. and H.P.; formal analysis, L.W. and J.W.; calculation, H.C.; experiment, Y.F. and C.W.; supervision, J.W. and H.P.; writing, L.W. and J.W. All authors have read and agreed to the published version of the manuscript.

Funding: This work was financially supported by the Natural Science Research Key Project of Anhui Provincial Department of Education (KJ2021A1036, Junbo Wang), Zhejiang Provincial Natural Science Foundation of China (LGF22B070005, Hua Pan), the College Students' Innovative Entrepreneurial Training Project (S202110375086, 202210375019, Junbo Wang), and the Special Innovation Foundation of Anhui Province (2020XZX005, Junbo Wang).

Data Availability Statement: Data are available from the authors.

Acknowledgments: We would like to thank Seyit YUZUAK for his assistance with language and grammar correction, editing, and advising, which greatly improved the manuscript.

Conflicts of Interest: The authors declare no conflict of interest.

References

1. Schipper, D.E.; Zhao, Z.; Leitner, A.P.; Xie, L.; Qin, F.; Alam, M.K.; Chen, S.; Wang, D.; Ren, Z.; Wang, Z.; et al. A $TiO_2/FeMnP$ core/shell nanorod array photoanode for efficient photoelectrochemical oxygen evolution. *ACS Nano* **2017**, *11*, 4051–4059. [CrossRef]
2. Li, S.J.; Hu, S.W.; Jiang, W.; Liu, Y.; Liu, J.S.; Wang, Z.H. Facile synthesis of flower-like Ag_3VO_4/Bi_2WO_6 heterojunction with enhanced visible-light photocatalytic activity. *J. Colloid Interface Sci.* **2017**, *501*, 156–163. [CrossRef]
3. Meng, F.P.; Liu, Y.Z.; Wang, J.; Tan, X.Y.; Sun, H.Q.; Liu, S.M.; Wang, S.B. Temperature dependent photocatalysis of $g\text{-}C_3N_4$, TiO_2 and ZnO: Differences in photoactive mechanism. *J. Colloid Interface Sci.* **2018**, *532*, 321–330. [CrossRef]
4. Yao, L.Z.; Wang, W.Z.; Wang, L.J.; Liang, Y.J.; Fu, J.L.; Shi, H.L. Chemical bath deposition synthesis of TiO_2/Cu_2O core/shell nanowire arrays with enhanced photoelectrochemical water splitting for H_2 evolution and photostability. *Int. J. Hydrogen Energy* **2018**, *43*, 15907–15917. [CrossRef]
5. Kosemen, A.; Kosemen, Z.A.; Canimkubey, B.; Erkovan, M.; Basarir, F.; San, S.E.; Ornek, O.; Tunc, A.V. Fe doped TiO_2 thin film as electron selective layer for inverted solar cells. *Sol. Energy* **2016**, *132*, 511–517. [CrossRef]
6. Zhang, F.J.; Zhu, S.F.; Xie, F.Z.; Zhang, J.; Meng, Z.D. Plate-on-plate structured Bi_2MoO_6/Bi_2WO_6 heterojunction with high-efficiently gradient charge transfer for decolorization of MB. *Sep. Purif. Technol.* **2013**, *113*, 1–8. [CrossRef]
7. Zhang, Y.H.; Zhang, N.; Tang, Z.R.; Xu, Y.J. Identification of Bi_2WO_6 as a highly selective visible-light photocatalyst toward oxidation of glycerol to dihydroxyacetone in water. *Chem. Sci.* **2013**, *4*, 1820–1824. [CrossRef]
8. Hill, J.C.; Choi, K.S. Synthesis and characterization of high surface area $CuWO_4$ and Bi_2WO_6 electrodes for use as photoanodes for solar water oxidation. *J. Mater. Chem. A* **2013**, *1*, 5006–5014. [CrossRef]

9. Zhang, Z.M.; Jiang, X.; Mei, J.F.; Li, Y.X.; Han, W.H.; Xie, M.Z.; Wang, F.C.; Xie, E.Q. Improved photoelectrocatalytic hydrogen generation through $BiVO_4$ quantum-dots loaded on nano-structured SnO_2 and modified with carbon quantum-dots. *Chem. Eng. J.* **2018**, *331*, 48–53. [CrossRef]
10. Nualkaew, P.; Phuruangrat, A.; Dumrongrojthanath, P.; Thongtem, S.; Thongtem, T. Synthesis of Ag_3VO_4 nanoparticles loaded on Bi_2MoO_6 nanoplates as heterostructure visible light driven photocatalyst by sonochemical method. *J. Ceram. Soc. Jpn.* **2016**, *124*, 1157–1160. [CrossRef]
11. Kumar, S.; Surendar, T.; Baruah, A.; Shanker, V. Synthesis of a novel and stable g-C_3N_4-Ag_3PO_4 hybrid nanocomposite photocatalyst and study of the photocatalytic activity under visible light irradiation. *J. Mater. Chem. A* **2013**, *1*, 5333–5340. [CrossRef]
12. Yan, Q.S.; Li, C.; Lin, C.P.; Zhao, Y.L.; Zhang, M.H. Visible light response $AgBr/Ag_3PO_4$ hybrid for removal of anionic dye and tetracycline hydrochloride in water. *J. Mater. Sci. Mater. Electron.* **2018**, *29*, 2517–2524. [CrossRef]
13. Qiao, R.; Mao, M.; Hu, E.; Zhong, Y.; Ning, J.; Hu, Y. Facile formation of mesoporous $BiVO_4/Ag/AgCl$ heterostructured microspheres with enhanced visible-light photoactivity. *Inorg. Chem.* **2015**, *54*, 9033–9039. [CrossRef] [PubMed]
14. Mei, F.F.; Dai, K.; Zhang, J.F.; Li, W.Y.; Liang, C.H. Construction of Ag SPR-promoted step-scheme porous g-C_3N_4/Ag_3VO_4 heterojunction for improving photocatalytic activity. *Appl. Surf. Sci.* **2019**, *488*, 151–160. [CrossRef]
15. Zhou, Y.G.; Zhang, Y.F.; Lin, M.S.; Long, J.L.; Zhang, Z.Z.; Lin, H.X.; Wu, J.C.S.; Wang, X.X. Monolayered Bi_2WO_6 nanosheets mimicking heterojunction interface with open surfaces for photocatalysis. *Nat. Commun.* **2015**, *6*, 8340. [CrossRef]
16. Qiu, L.Y.; Cui, Y.M.; Tan, X.Y.; Zheng, S.X.; Zhang, H.; Xu, J.W.; Wang, Q.Y. Construction of $Ag_3PO_4/Ag_4P_2O_7$ nanospheres sensitized hierarchical titanium dioxide nanotube mesh for photoelectrocatalytic degradation of methylene blue. *Sep. Purif. Technol.* **2019**, *215*, 619–624. [CrossRef]
17. Vattikuti, S.V.P.; Zeng, J.; Ramaraghavulu, R.; Shim, J.; Mauger, A.; Julien, C.M. High-Throughput Strategies for the Design, Discovery, and Analysis of Bismuth-Based Photocatalysts. *Int. J. Mol. Sci.* **2022**, *24*, 663. [CrossRef]
18. Wang, R.; Xu, M.; Xie, J.W.; Ye, S.Y.; Song, X.L. A spherical TiO_2-Bi_2WO_6 composite photocatalyst for visible-light photocatalytic degradation of ethylene. *Colloid Surface A* **2020**, *602*, 125048. [CrossRef]
19. Huang, C.; Chen, L.; Li, H.; Mu, Y.; Yang, Z. Synthesis and application of Bi_2WO_6 for the photocatalytic degradation of two typical fluoroquinolones under visible light irradiation. *RSC Adv.* **2019**, *9*, 27768–27779. [CrossRef]
20. Wang, J.J.; Tang, L.; Zeng, G.M.; Deng, Y.C.; Liu, Y.N.; Wang, L.G.; Zhou, Y.Y.; Guo, Z.; Wang, J.J.; Zhang, C. Atomic scale g-C_3N_4/Bi_2WO_6 2D/2D heterojunction with enhanced photocatalytic degradation of ibuprofen under visible light irradiation. *Appl. Catal. B Environ.* **2017**, *209*, 285–294. [CrossRef]
21. Lu, X.Y.; Che, W.J.; Hu, X.F.; Wang, Y.; Zhang, A.T.; Deng, F.; Luo, S.L.; Dionysiou, D.D. The facile fabrication of novel visible-light-driven Z-scheme $CuInS_2/Bi_2WO_6$ heterojunction with intimate interface contact by in situ hydrothermal growth strategy for extraordinary photocatalytic performance. *Chem. Eng. J.* **2019**, *356*, 819–829. [CrossRef]
22. Ma, F.Y.; Yang, Q.L.; Wang, Z.J.; Liu, Y.H.; Xin, J.J.; Zhang, J.J.; Hao, Y.T.; Li, L. Enhanced visible-light photocatalytic activity and photostability of Ag_3PO_4/Bi_2WO_6 heterostructures toward organic pollutant degradation and plasmonic Z-scheme mechanism. *RSC Adv.* **2018**, *8*, 15853–15862. [CrossRef] [PubMed]
23. Chen, X.J.; Dai, Y.Z.; Wang, X.Y. Methods and mechanism for improvement of photocatalytic activity and stability of Ag_3PO_4: A review. *J. Alloys Compd.* **2015**, *649*, 910–932. [CrossRef]
24. Jonjana, S.; Phuruangrat, A.; Thongtem, T.; Kuntalue, B.; Thongtem, S. Decolorization of rhodamine B photocatalyzed by Ag_3PO_4/Bi_2WO_6 nanocomposites under visible radiation. *Mater. Lett.* **2018**, *218*, 146–149. [CrossRef]
25. Ma, P.Y.; Yu, Y.; Xie, J.J.; Fu, Z.Y. Ag_3PO_4/CuO composites utilizing the synergistic effect of photocatalysis and Fenton-like catalysis to dispose organic pollutants. *Adv. Powder Technol.* **2017**, *28*, 2797–2804. [CrossRef]
26. Zheng, C.X.; Yang, H. Assembly of Ag_3PO_4 nanoparticles on rose flower-like Bi_2WO_6 hierarchical architectures for achieving high photocatalytic performance. *J. Mater. Sci. Mater. Electron.* **2018**, *29*, 9291–9300. [CrossRef]
27. Amiri, M.; Dashtian, K.; Ghaedi, M.; Mosleh, S.; Jannesar, R. Bi_2WO_6/Ag_3PO_4-Ag Z-scheme heterojunction as a new plasmonic visible-light-driven photocatalyst: Performance evaluation and mechanism study. *New J. Chem.* **2019**, *43*, 1275–1284. [CrossRef]
28. Qian, X.F.; Yue, D.T.; Tian, Z.Y.; Reng, M.; Zhu, Y.; Kan, M.; Zhang, T.Y.; Zhao, Y.X. Carbon quantum dots decorated Bi_2WO_6 nanocomposite with enhanced photocatalytic oxidation activity for VOCs. *Appl. Catal. B Environ.* **2016**, *193*, 16–21. [CrossRef]
29. Hou, G.Q.; Zeng, X.F.; Gao, S.J. Fabrication and photocatalytic activity of core@shell $Ag_3PO_4@Cu_2O$ heterojunction. *Mater. Lett.* **2019**, *238*, 116–120. [CrossRef]
30. Chi, C.Y.; Pan, J.Q.; You, M.Z.; Dong, Z.J.; Zhao, W.J.; Song, C.S.; Zheng, Y.Y.; Li, C.R. The porous TiO_2 nanotubes/Ag_3PO_4 heterojunction for enhancing sunlight photocatalytic activity. *J. Phys. Chem. Solids* **2018**, *114*, 173–178. [CrossRef]
31. Zhang, F.J.; Sun, R.; Li, R.S.; Song, N.N.; Feng, L.M.; Zhong, S.; Zhao, Z.Q. Novel La-doped Bi_2WO_6 photocatalysts with enhanced visible-light photocatalytic activity. *J. Sol-Gel Sci. Technol.* **2018**, *86*, 640–649. [CrossRef]
32. Zhang, J.L.; Ma, Z. Ag_3VO_4/AgI composites for photocatalytic degradation of dyes and tetracycline hydrochloride under visible light. *Mater. Lett.* **2018**, *216*, 216–219. [CrossRef]
33. Liu, Y.; Wang, W.G.; Si, M.Z.; Yu, Y.F.; Zhang, H.Y. (Yb^{3+}, Er^{3+}) co-doped TiO_2/Ag_3PO_4 hybrid photocatalyst with enhanced activity for photodegradation of phenol. *Appl. Surf. Sci.* **2019**, *463*, 159–168. [CrossRef]

34. Tian, L.; Xian, X.Z.; Cui, X.K.; Tang, H.; Yang, X.F. Fabrication of modified g-C_3N_4 nanorod/Ag_3PO_4 nanocomposites for solar-driven photocatalytic oxygen evolution from water splitting. *Appl. Surf. Sci.* **2018**, *430*, 301–308. [CrossRef]
35. Shen, Y.Z.; Zhu, Z.D.; Wang, X.G.; Khan, A.; Gong, J.Y.; Zhang, Y.R. Synthesis of Z-scheme g-C_3N_4/Ag/Ag_3PO_4 composite for enhanced photocatalytic degradation of phenol and selective oxidation of gaseous isopropanol. *Mater. Res. Bull.* **2018**, *107*, 407–415. [CrossRef]